Nonlinear Modeling of the Inverse Force Function for the Planar Switched Reluctance Motor Using Sparse Least Squares Support Vector Machines

Su-Dan Huang, Guang-Zhong Cao, *Member, IEEE*, Zheng-You He, *Senior Member, IEEE*, J. F. Pan, Ji-An Duan, and Qing-Quan Qian

Abstract—In the advanced manufacturing industry, planar switched reluctance motors (PSRMs) have proved to be a promising candidate due to their advantages of high precision, low cost, low heat loss, and ease of manufacture. However, their inverse force function, which provides vital phase current command for precise motion, is highly nonlinear and hard to be accurately modeled. This paper proposes a novel inverse force function using sparse least squares support vector machines (LS-SVMs) to achieve nonlinear modeling for precise motion of a PSRM. The required training and testing sets of sparse LS-SVMs are first obtained from experimental measurement. A sparse LS-SVMs regression is further developed using training set to accurately model the inverse force function. Accordingly, the function is tested via the testing set to assess its feasibility. Finally, the proposed approach is applied to the PSRM system with dSPACE controller for trajectory tracking, and its effectiveness and superior performance are verified through experimental results.

Index Terms—Inverse force function, least squares support vector machines (LS-SVMs), nonlinear modeling, phase current estimation, planar switched reluctance motors (PSRMs).

I. INTRODUCTION

R ECENTLY, with the rapid progress in advanced manufacturing industry, the direct drive planar motors attract increasing attention since they feature simple structure, high

S.-D. Huang is with the Department of Electrical Engineering, Southwest Jiaotong University, Chengdu 610031, China, and also with the Shenzhen Key Laboratory of Electromagnetic Control, Shenzhen University, Shenzhen 518060, China (e-mail: hsdsudan@gmail.com).

G.-Z. Cao and J. F. Pan are with the Shenzhen Key Laboratory of Electromagnetic Control, Shenzhen University, Shenzhen 518060, China (e-mail: gzcao.01@gmail.com; pan_jian_fei@163.com).

Z.-Y. He and Q.-Q. Qian are with the Department of Electrical Engineering, Southwest Jiaotong University, Chengdu 610031, China (e-mail: hezy@swjtu.edu.cn; qqq@swjtu.edu.cn).

J.-A. Duan is with the State Key Laboratory of High Performance Complex Manufactory, Central South University, Changsha 410083, China (e-mail: duanjian@mail.csu.edu.cn).

Color versions of one or more of the figures in this paper are available online at http://ieeexplore.ieee.org.

Digital Object Identifier 10.1109/TII.2015.2411438

reliability, low friction, and no backlash compared with the conventional planar motors with cumbersome mechanical transmission mechanism [1]–[7]. The direct drive planar switched reluctance motors (PSRMs) derived from linear switched reluctance motors (LSRMs) are an attractive candidate in high-precision two-dimensional (2-D) positioning device, owing to their advantages of high precision, low cost, low heat loss, ease of manufacture, and strong adaptability of harsh environment [7], [8].

In the control strategy of PSRMs, there is inverse force function which is inverse function of thrust force. The inverse force function provides phase current command to current driver for achieving planar motion in terms of the inputs of the position from linear encoder and thrust force command from position controller [7], [8]. Therefore, accurate modeling of the inverse force function plays a key role in providing precise phase current command for precise motion of PSRMs. However, the inverse force function is highly nonlinear and hard to be accurately modeled due to the inherently complex magnetic characteristic of PSRMs.

The inverse force function of LSRMs is directly applied to that of PSRMs so far. There are primarily two methods used to model the inverse force function. The first method is to deduce the inverse force function from a thrust force function based on the linear magnetic field under low-phase current level, and it is frequently employed in literatures [9]–[12]. Nevertheless, applying this method is hugely limited, since it fails to provide precise phase current command in the case of nonlinear magnetic field in which PSRMs frequently operate. Moreover, appropriate and valid control algorithm has to be designed to achieve more precise motion by using this method. Consequently, not only the complexity of the control system would be increased but also the application of high-precision motion of PSRMs would be limited. The second method utilizes a lookup table to model the inverse force function [7], [13]. A current–force–position lookup table is constructed from static experimental data, and an interpolation method is adopted to calculate the phase current command based on the lookup table. However, using this method, not only high memory capacity is required for processor employed in control but also low-precision phase current command is obtained with meager experimental data. Hence, in order to provide precise phase current command for precise motion of PSRMs, the inverse force function to deal with accurate nonlinear modeling is

in high demand, and it is one of the problems to be solved urgently.

As for switched reluctance motors, artificial neural networks (ANNs) have been successfully employed to nonlinear modeling of flux linkage with respect to phase current and rotor position [14], [15], owing to their ability to model the nonlinear characteristics. However, the systematic approach concerning how to decide the number of hidden layers and neurons has not been fully proposed. Meanwhile, ANNs also exhibit shortcomings of overfitting, requiring large sample, and sinking into local optima. Alternatively, it has been demonstrated that support vector machines (SVMs) provide an effective approach to avoid the aforementioned problems of ANNs, which are a new machine learning method for classification and regression based on statistical learning theory and structural risk minimization principle [16]–[20]. SVMs have been effectively applied in function estimation [21]–[23], fault diagnose [24], [25], data mining [26], [27], and speech recognition [28], [29]. Furthermore, least squares SVMs (LS-SVMs) possess faster arithmetic speed compared to SVMs [30]. Since the sparseness is lost in LS-SVMs compared with SVMs, sparse LS-SVMs have been proposed to impose the sparseness of LS-SVMs [31]. As aforementioned analysis, sparse LS-SVMs are a powerful tool for nonlinear modeling.

For high-precision planar motion of PSRMs, it is noticeable that sparse LS-SVMs are a good choice to nonlinear modeling of the inverse force function, since they are capable of solving nonlinearity, overfitting, small sample, local optima, low arithmetic speed, and requirement of high memory capacity for processor. Thus, a novel nonlinear inverse force function of a PSRM using sparse LS-SVMs is proposed in this paper. The training and testing of the function are further performed, and the involved experiments are carried out to validate the effectiveness of the proposed approach.

II. SYSTEM DESCRIPTION

A. Structure

PSRMs are variable reluctance motors based on the minimum reluctance principle, which have doubly salient and are energized by dc current. PSRMs can be considered as two LSRMs with orthogonal magnetic circuits.

The experimental setup of the PSRM system is presented in Fig. 1(a) in which the PSRM developed in our laboratory is shown. The specifications of the PSRM are listed in Table I. The PSRM consists of stator sets, X and Y moving platforms, X- and Y-axes linear encoders, X- and Y-axes linear guides, stator base, etc. For achieving planar motion, two pairs of linear guide are applied to support linear motions in X- and Y-axes. Fig. 1(b) shows the structures of one stator block, combination of four stator blocks, one mover, and X moving platform. The stator block is constituted by a set of laminated silicon steels, the stator sets constructed from combination of four stator blocks are mesh structure, and one mover with six teeth is composed of a set of laminated silicon steels. The Y moving platform consists of the moving slider and the X moving platform, and the X moving platform consists of two sets of three identical movers with
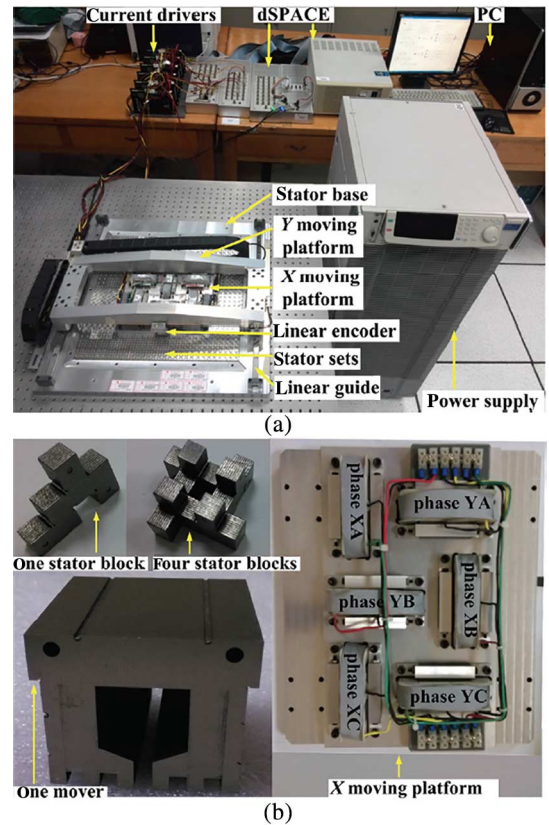

Fig. 1. (a) Experimental setup of the PSRM system. (b) Structures of stator block, combination of four stator blocks, mover, and X moving platform.

TABLE I
SPECIFICATIONS OF THE PSRM

Parameters	Value
Tooth width of movers and stators	3.6 mm
Pole pitch of movers and stators	7.2 mm
Mass of one stator	0.002 kg
Mass of stator sets	7.2 kg
Mass of one mover	0.3462 kg
Mass of X moving platform	5.9 kg
Mass of Y moving platform	13.9 kg
Mass of the PSRM	55.4 kg
Airgap length	0.3 mm
Range of base plate	600 mm × 600 mm
Resolution of encoders	100 nm, 50 nm
Phase resistance	0.5 Ω
Number of turns per phase	150

three-phase winding. The two sets of movers are perpendicular to each other, and each set of movers is responsible for the motion in each axis. Phase XA, XB, and XC and phase YA, YB, and YC are three-phase winding in X- and Y-axes, respectively. Due to the perpendicular arrangement of two sets, the two sets of three-phase winding are decoupled magnetically.
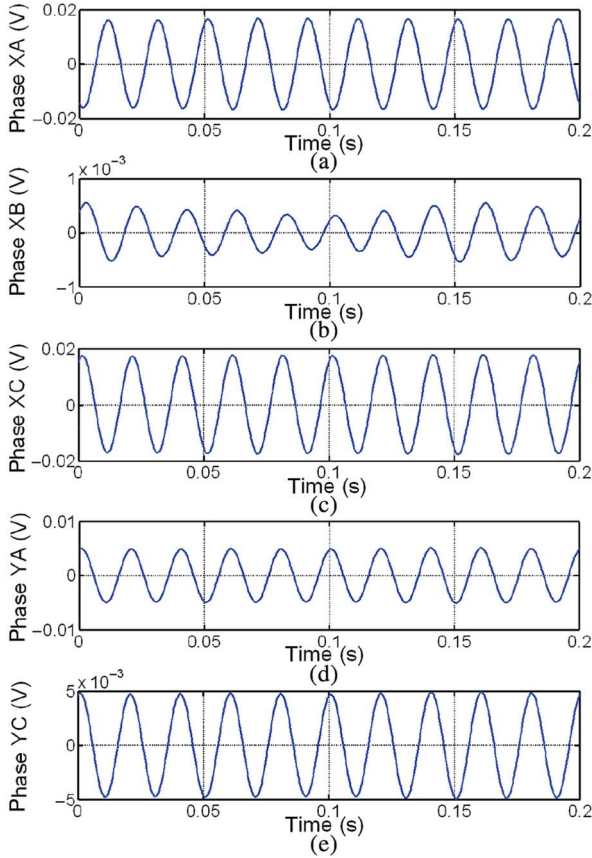
Fig. 2. Induced voltages. (a) Phase *XA*. (b) Phase *XB*. (c) Phase *XC*. (d) Phase *YA*. (e) Phase *YC*.
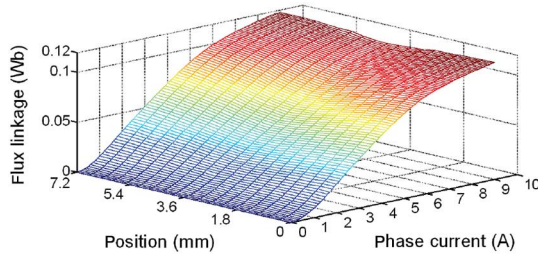

Fig. 3. Flux linkage versus phase current versus position from experimental data.

B. Modeling

Fig. 2 manifests the induced voltages of remaining phase windings when phase *YB* of the PSRM is energized by a sinusoidal voltage with 3-V amplitude and 50-Hz frequency. From Fig. 2, it is clear that the two sets of movers are virtually decoupled magnetically since these induced voltages are almost zero. As a result, electromagnetic forces of two axes are independently generated with little mutual influence. For phase *YB* of the PSRM, the flux linkage versus phase current versus position in a pole pitch from experimental data is demonstrated in Fig. 3. Fig. 3 demonstrates the nonlinear and complex magnetic field of the PSRM. Thus, the PSRM is a highly nonlinear system, and it is hard to formulate the accurate model of the PSRM.

For phase k of l-axis, the voltage balance equation is given by

$$
\begin{aligned}
u_{lk} &= R_{lk}i_{lk} + \frac{\partial \lambda_{lk}(i_{lk}, x_l)}{\partial t} \\
&= R_{lk}i_{lk} + \frac{\partial \lambda_{lk}(i_{lk}, x_l)}{\partial x_l}\frac{\partial x_l}{\partial t} + \frac{\partial \lambda_{lk}(i_{lk}, x_l)}{\partial i_{lk}}\frac{\partial i_{lk}}{\partial t} \\
&= R_{lk}i_{lk} + i_{lk}\frac{\partial L_{lk}(i_{lk}, x_l)}{\partial x_l}\frac{\partial x_l}{\partial t} + L_{lk}(i_{lk}, x_l)\frac{\partial i_{lk}}{\partial t}
\end{aligned} \tag{1}
$$
$$l = X, Y, k = A, B, C$$

where x_l is the position of l-axis, u_{lk}, i_{lk}, R_{lk}, λ_{lk}, and L_{lk} are the phase voltage, the phase current, the phase resistance, the flux linkage, and the inductance of phase k in l-axis, respectively.

For l-axis, the mechanical movement equation is given as

$$f_l = m_l \frac{d^2 x_l}{dt^2} + b_l \frac{dx_l}{dt} + f_{lp} + f_{lu} \tag{2}$$

where $m_l, b_l, f_{lp}, f_{lu},$ and f_l are the mass of moving platform, the damping coefficient, the external load force, the friction, and the electromagnetic thrust force of l-axis, respectively.

For the case of constant excitation of phase k in l-axis, the incremental mechanical energy ∂W_{lk} is equal to the rate of change of co-energy $\partial W'_{lk}$, where W_{lk} is the mechanical energy and W'_{lk} is the co-energy which is nothing but the complement of the field energy [32]. Hence

$$\partial W_{lk} = \partial W'_{lk} \tag{3}$$

where

$$W'_{lk} = \int \lambda_{lk}(i_{lk}, x_l)di_{lk} = \int L_{lk}(i_{lk}, x_l)i_{lk}di_{lk}. \tag{4}$$

Therefore, the electromagnetic thrust force of l-axis in terms of the mechanical energy is expressed as

$$
\begin{aligned}
f_l &= \sum_{k=A}^{C} f_{lk} = \sum_{k=A}^{C} \frac{\partial W_{lk}}{\partial x_l} = \sum_{k=A}^{C} \left.\frac{\partial W'_{lk}}{\partial x_l}\right|_{i_{lk}=\tau_{lk}} \\
&= \sum_{k=A}^{C} \frac{\partial \int_0^{\tau_{lk}} \lambda_{lk}di_{lk}}{\partial x_l}
\end{aligned} \tag{5}
$$

where f_{lk} and τ_{lk} are the electromagnetic thrust force and the constant phase current of phase k in l-axis, respectively.

For the linear magnetic field under low-phase current level, the electromagnetic thrust force can be approximately derived as [32]

$$f_l = \sum_{k=A}^{C} \frac{1}{2}\frac{dL_{lk}}{dx_l}i_{lk}^2. \tag{6}$$

Additionally, the inverse force function is an inverse function of thrust force. In terms of (5), for phase k in l-axis of the PSRM, the nonlinear inverse force function is a function of the position of l-axis and thrust force of phase k in l-axis, which outputs the phase current of phase k in l-axis.
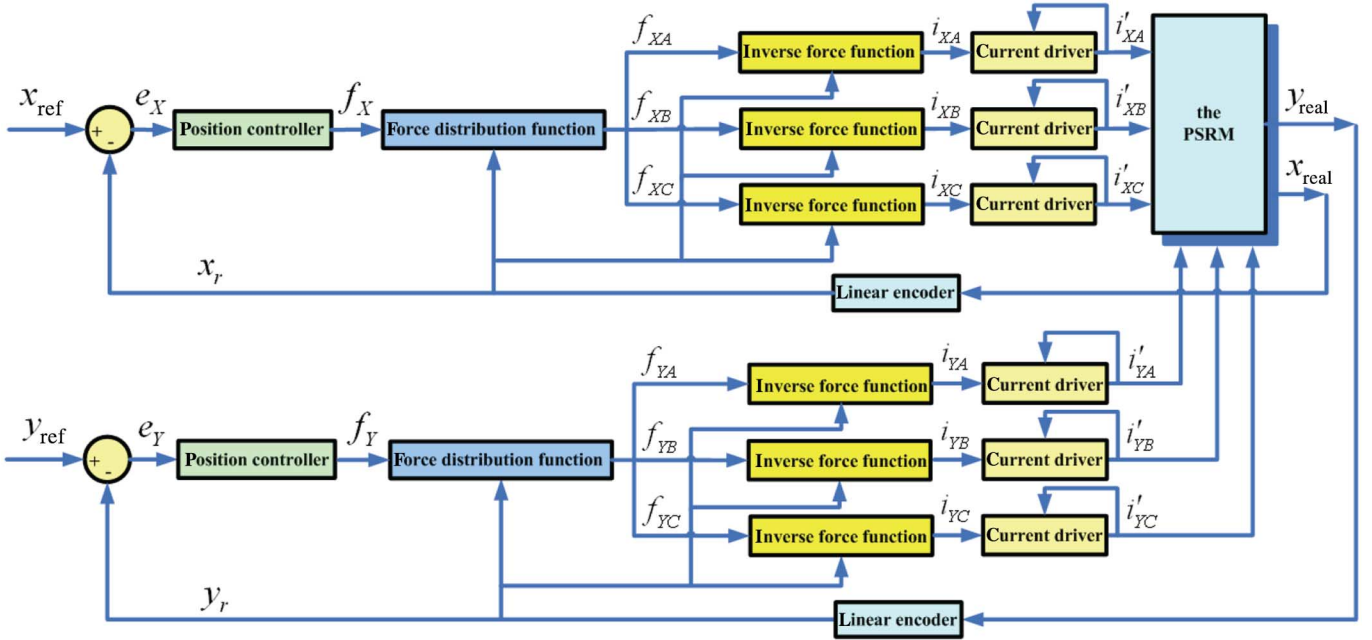
Fig. 4. Block diagram of the PSRM control system.

C. Control Strategy

The block diagram of the PSRM control system is shown in Fig. 4. Since 2-D motions of the PSRM are virtually decoupled, two standalone controllers are applied to linear motions of two axes, respectively. For the linear motion of X-axis, the real position x_{real} is detected and transformed into the position signal x_r by a linear encoder. The position signal x_r is compared with the reference position signal x_{ref}, and their corresponding position error e_x is processed through a position controller to produce the thrust force command f_X. The thrust force commands of each phase f_{XA}, f_{XB}, and f_{XC} are produced by force distribution function (FDF) [11] according to the thrust force command f_X and the position signal x_r. With the position signal x_r and the thrust force commands of each phase f_{XA}, f_{XB}, and f_{XC}, the three-phase current command i_{XA}, i_{XB}, and i_{XC} are obtained via inverse force functions. The three-phase current command i_{XA}, i_{XB}, and i_{XC} and three-phase current i'_{XA}, i'_{XB}, and i'_{XC} are processed through current drivers to provide phase currents to the PSRM for achieving linear motion in X-axis.

III. NONLINEAR MODELING OF THE INVERSE FORCE FUNCTION BY SPARSE LS-SVMs

To obtain precise phase current commands of the PSRM, a nonlinear modeling of inverse force function under nonlinear magnetic field is proposed in this section. The inverse force function of phase k in l-axis is given as

$$i_{lk} = g(s) = g(x_l, f_{lk}) \qquad (7)$$

where $s = \{x_l, f_{lk}\}$ and i_{lk} are the input and output of the inverse force function, respectively.

In terms of (6), the inverse force function of phase k in l-axis under linear magnetic field is represented as

$$
\begin{aligned}
i_{lk} = g(s) &= g(x_l, f_{lk}) \\
&= \sqrt{2f_{lk}\left(\frac{dL_{lk}}{dx_l}\right)^{-1}}, \quad l = X, Y, \quad k = A, B, C.
\end{aligned}
\qquad (8)
$$

Since the PSRM operates in nonlinear magnetic field in most cases, the inverse force function is difficult to be accurately modeled to deal with the nonlinear magnetic characteristic according to (5). Based on sparse LS-SVMs, a regression function is adopted to model the inverse force function of phase k in l-axis with the training set obtained from experimental measurement under nonlinear magnetic field.

A. LS-SVMs Regression

LS-SVMs regression has the feature of establishing nonlinear system by mapping the input data into a high-dimensional feature space and then solving the regression problem of linear equations. The unknown regression function is expressed by

$$y^* = f(\boldsymbol{x}) = (\boldsymbol{w}, \varphi(\boldsymbol{x})) + b \qquad (9)$$

with the given training set $\{\boldsymbol{x}_j, y_j\}_{j=1}^h$, where $\boldsymbol{x}_j \in \boldsymbol{R}^n$ is the input data from training set, $y_j \in \boldsymbol{R}$ is the output data from training set, h is the number of training set, $y^* \in \boldsymbol{R}$ is the output of the function, $\varphi(.) : \boldsymbol{R}^n \to \boldsymbol{R}^d$ is a nonlinear map from the input vector to a higher dimensional feature space with dimension d, and $\boldsymbol{w} \in \boldsymbol{R}^n$ and $b \in \boldsymbol{R}$ are the parameters that control the function. $\boldsymbol{w}$ is defined as the weight vector and it denotes a direction perpendicular to the hyperplane which is an affine subspace of dimension $n - 1$, and b represents the bias with respect to the origin.

The mapping function $\varphi(\boldsymbol{x})$ is seldom explicitly known. In order to avoid the explicit computation of $\varphi(\boldsymbol{x})$ in the high-dimensional feature space, a kernel function is introduced to map the input vector implicitly into a feature space and to train a linear machine in such a space, potentially side-stepping the computational problems inherent in evaluating the feature map [16]. The kernel function is formulated as

$$K(\boldsymbol{x}_j, \boldsymbol{x}) = \varphi^T(\boldsymbol{x}_j)\varphi(\boldsymbol{x}), \quad j \in h. \tag{10}$$

The commonly used kernel functions are radial basis function (RBF), inhomogeneous polynomial kernel, and homogeneous polynomial kernel. The RBF is chosen for the kernel function of the LS-SVMs, which is expressed as

$$K(\boldsymbol{x}_j, \boldsymbol{x}) = \exp\left(-\frac{\|\boldsymbol{x}_j - \boldsymbol{x}\|^2}{\sigma^2}\right), \quad j \in h \tag{11}$$

where $\sigma > 0$ is the parameter that is closely associated with the generalization performance of LS-SVMs, and $\|\cdot\|$ is the Euclidean distance.

To obtain the parameters $\boldsymbol{w}$ and b, LS-SVMs regression is transformed into the optimization problem expressed as

$$\min_{\boldsymbol{w},b,\boldsymbol{e}} J(\boldsymbol{w}, \boldsymbol{e}) = \frac{1}{2}\boldsymbol{w}^T\boldsymbol{w} + \frac{1}{2}C\sum_{j=1}^{h} e_j^2 \tag{12}$$

$$\text{s.t. } y_j = (\boldsymbol{w}, \varphi(\boldsymbol{x}_j)) + b + e_j, \quad j = 1, 2, \ldots, h$$

where $J(\boldsymbol{w}, \boldsymbol{e})$ is a loss function, e_j is the error between y_j^* and y_j, and $C > 0$ is the penalty factor that determines a tradeoff between model complexity and empirical risk.

For solving the optimization problem, the Lagrangian function of (12) is given by

$$L(\boldsymbol{w}, b, \boldsymbol{e}, \boldsymbol{\alpha}) = \frac{1}{2}\boldsymbol{w}^T\boldsymbol{w} + \frac{1}{2}C\sum_{j=1}^{h} e_j^2$$
$$- \sum_{j=1}^{h} \alpha_j((\boldsymbol{w}, \varphi(\boldsymbol{x}_j)) + b + e_j - y_j) \tag{13}$$

where the coefficient $\alpha_j \in \boldsymbol{R}$ is the Lagrange multiplier. The Lagrange multiplier reflects the sparseness of SVMs, since the zero Lagrange multiplier makes no contribution to the solution of SVMs.

The Karush–Kuhn–Tuker (KKT) conditions for optimality of (13) are

$$\begin{cases} \dfrac{\partial L}{\partial \boldsymbol{w}} = 0 \rightarrow \boldsymbol{w} = \sum_{j=1}^{h} \alpha_j \varphi(\boldsymbol{x}_j) \\ \dfrac{\partial L}{\partial b} = 0 \rightarrow \sum_{j=1}^{h} \alpha_j = 0 \\ \dfrac{\partial L}{\partial \boldsymbol{e}} = 0 \rightarrow \alpha_j = C e_j \\ \dfrac{\partial L}{\partial \boldsymbol{\alpha}} = 0 \rightarrow (\boldsymbol{w}, \varphi(\boldsymbol{x}_j)) + b + e_j - y_j = 0. \end{cases} \tag{14}$$

Equation (14) can be rewritten as the solution to the linear equations formulated as

$$\begin{bmatrix} 0 & \boldsymbol{d}^T \\ \boldsymbol{d} & \boldsymbol{Q} + C^{-1}\boldsymbol{I} \end{bmatrix} \begin{bmatrix} b \\ \boldsymbol{\eta} \end{bmatrix} = \begin{bmatrix} 0 \\ \boldsymbol{\beta} \end{bmatrix} \tag{15}$$
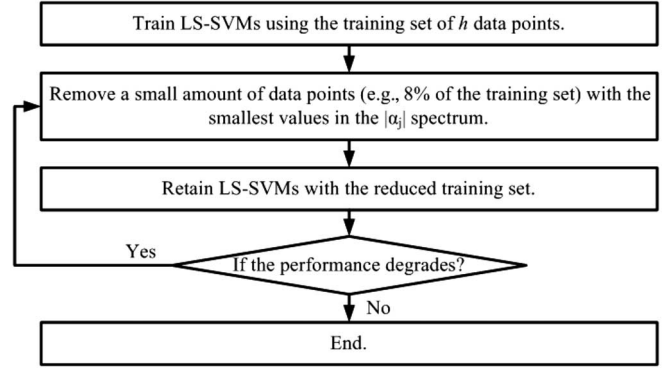

Fig. 5. Flowchart of the algorithm for sparse LS-SVMs.

where $\boldsymbol{d}^T = [1, 1, \ldots, 1] \in \boldsymbol{R}^h$, $\boldsymbol{\eta}^T = [\alpha_1, \alpha_2, \ldots, \alpha_h] \in \boldsymbol{R}^h$, $\boldsymbol{\beta}^T = [y_1, y_2, \ldots, y_h] \in \boldsymbol{R}^h$, $\boldsymbol{I} = \text{diag}(1, 1, \ldots, 1) \in \boldsymbol{R}^{h \times h}$ is an identity matrix, and $\boldsymbol{Q} \in \boldsymbol{R}^{h \times h}$ is expressed as

$$Q_{rj} = K(\boldsymbol{x}_r, \boldsymbol{x}_j) = \varphi^T(\boldsymbol{x}_r)\varphi(\boldsymbol{x}_j), \quad r, j \in h. \tag{16}$$

To establish the regression function, parameters C and σ must be determined. With the training set $\{\boldsymbol{x}_j, y_j\}_{j=1}^{h}$, parameters C and σ are calculated by the tenfold cross-validation method which is the most commonly used cross-validation method. Cross-validation method is an intuitive technique for estimating the accuracy of theories learned by machine learning algorithm, which is frequently applied to modeling and can be a useful method for choosing tuning parameters of regression [33].

With the calculated parameters C and σ, b and α_j are obtained by solving (15). Then, the LS-SVMs regression function is deduced and represented as

$$y^* = \sum_{j=1}^{h} \alpha_j \varphi^T(\boldsymbol{x}_j)\varphi(\boldsymbol{x}) + b = \sum_{j=1}^{h} \alpha_j K(\boldsymbol{x}_j, \boldsymbol{x}) + b. \tag{17}$$

B. Sparse LS-SVMs

The standard SVMs achieve the sparseness because they have a number of zero Lagrange multipliers. However, the sparseness is lost in LS-SVMs due to their all nonzero Lagrange multipliers. Sparse LS-SVMs are proposed to impose sparseness of LS-SVMs. For sparse LS-SVMs, LS-SVMs are retrained with the remaining data points, while the least important data points of training set are omitted. The flowchart of the algorithm for sparse LS-SVMs is manifested in Fig. 5 [31].

Using the training set, parameters C and σ, and the solution of (15), a sparse LS-SVMs is trained based on the algorithm described in Fig. 5. Then, the sparse LS-SVMs are built after training.

C. Training and Testing of the Inverse Force Function

For the phase *YB* of the PSRM, experimental measurement of thrust force versus phase current from 0 to 10 A versus position in a pole pitch is performed to obtain the sample set of the sparse LS-SVMs. The acquired experimental data with 500 data
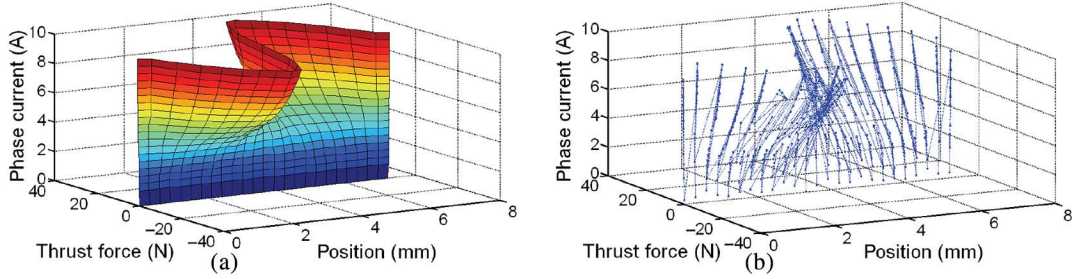
Fig. 6. Phase current versus thrust force versus position. (a) Experimental data points. (b) Data points from the inverse force function.
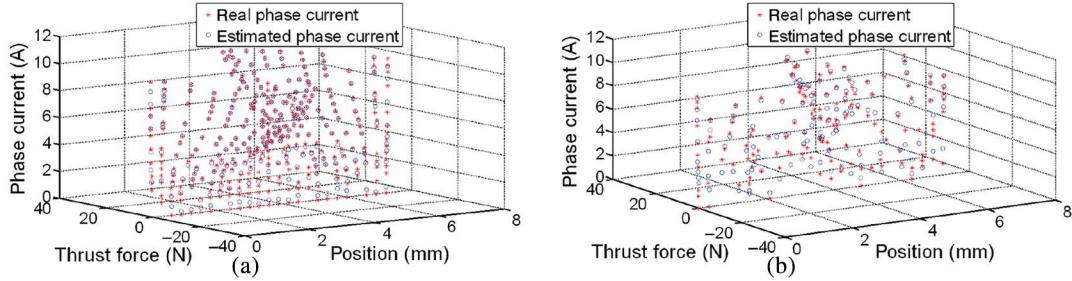

Fig. 7. Estimated phase current and real phase current. (a) Training output. (b) Testing output.

points are adopted as the sample set, which describes the nonlinear characteristic of thrust force, phase current, and position in a pole pitch. The experimental data of thrust force and position are employed as the input data of the sparse LS-SVMs, while the experimental data of phase current are utilized as the output data. For the sample set, the 350 data points randomly selected are used as the training set to build the sparse LS-SVMs for the inverse force function, and the remaining 150 data points are applied as the testing set to assess the generalization performance of the sparse LS-SVMs. The highly nonlinear relationship of the experimental data points is shown in Fig. 6(a) where stator and mover teeth completely overlapped is selected as the original position. To assess the learning and generalization performances, the root-mean-square error of the sparse LS-SVMs is defined as

$$e_{rms} = \sqrt{\frac{1}{N} \sum_{j=1}^{N} e_j^2} \qquad (18)$$

where e_j is the error between the phase current from the experimental data points and the corresponding estimated phase current from the output of the sparse LS-SVMs, and N is the number of training or testing data points.

Based on MATLAB, the parameters $C = 150$ and $\sigma = 0.03$ are obtained with the given training set by the tenfold cross-validation method, and then the parameters C and σ are applied to train the sparse LS-SVMs to calculate the values of b and α_j using the given training set. The sparse LS-SVMs are built after the training process is completed. That is, the built sparse LS-SVMs are the inverse force function of the PSRM. The relationship of phase current, position, and thrust force from the inverse force function is illustrated in Fig. 6(b). Compared with Fig. 6(a) and (b), it is clear that the phase current from experimental data points is consistent with that from the inverse

force function, and it also shows the feasibility of the inverse force function to estimate the phase current of the PSRM. The training and testing outputs of the inverse force function are demonstrated in Fig. 7(a) and (b), respectively. In addition, the root-mean-square errors of training and testing are 0.3269 and 0.6266 A, respectively. Concerning Fig. 7 and these root-mean-square errors, it is observed that the inverse force function has small training error and testing error except that the estimated phase current is less than 1 A. For the PSRM, the operating current mainly works ranging from 2 to 6 A. Therefore, the inverse force function based on the sparse LS-SVMs is appropriate for planar motion of the PSRM.

IV. EXPERIMENTAL VERIFICATION

A. Experimental Setup

The experimental setup of the PSRM system is depicted in Fig. 1(a). The system is composed of the PSRM, dSPACE controller, current drivers, linear optical encoders, PC, and power supply. Two Renishaw's linear optical encoders of Tonic series with dual resolution of 100 and 50 nm are applied to detect the position of X- and Y-axes. Six 50A20 servo drives from advanced motion controls (AMC) are used as current drivers to provide dc phase currents to the PSRM. The control algorithm is developed under MATLAB/Simulink, and it is downloaded to dSPACE modular hardware by real-time-workspace (RTW) and real-time-interface (RTI) for achieving real-time control. The utilized dSPACE modular hardware includes DS1005 PPC board, DS3001 incremental encoder interface board, and DS2103 D/A board. DS1005 PPC board is one of the processor boards of dSPACE running at 1 GHz. DS3001 incremental encoder interface board with six incremental encoder interface channels and 32-bit position counter is used to collect the position signals of the PSRM from linear optical encoders.

DS2103 D/A board with 32 parallel D/A converters, 16-bit resolution, and 1.6-μs sample time is provided to output phase current commands to current drivers. ControlDesk is one of the software of dSPACE, and is employed to data collection and parameter managing of the PSRM system.

B. Experimental Results

The developed inverse force function and two PD controllers are applied to the PSRM system for circular and quinquangular trajectory tracking. For circular and quinquangular trajectory tracking, the sampling time of the control algorithm is 0.001 s, and phase current command is limited to 8 A in the control algorithm. For circular trajectory tracking, parameters of PD controller in X-axis are $k_{px} = 250$ and $k_{dx} = 1.21$, and those in Y-axis are $k_{py} = 300$ and $k_{dy} = 0.86$. A circular trajectory with 100 mm diameter and 0.2 Hz frequency is used as the reference trajectory, where a reference signal of sinusoidal waveform with 50 mm amplitude and 0.2 Hz frequency is applied in X-axis, and a waveform of cosine with 50 mm amplitude and 0.2 Hz frequency is employed as the reference signal in Y-axis. For quinquangular trajectory tracking, parameters of PD controller in X-axis are $k_{px} = 191$ and $k_{dx} = 0.76$, and those in Y-axis are $k_{py} = 278$ and $k_{dy} = 0.82$. For linear motion in X-axis, a reference signal of continuous waveform with maximum amplitude of 60 mm and 1/6 Hz frequency is applied. A continuous waveform with maximum amplitude of 57 mm and 1/6 Hz frequency is used as the reference signal in Y-axis.

The phase current commands of X- and Y-axes for circular trajectory tracking are indicated in Fig. 8, while those for quinquangular trajectory tracking are presented in Fig. 9. As shown in Figs. 8 and 9, the inverse force function is capable of providing continuous phase current command in real time, phase current commands of both axes for both trajectory tracking are bounded on [0A 8A], and they mainly run ranging from 2 to 4 A. That is, the PSRM system mainly works at nonlinear magnetic field, since the linear magnetic field runs under phase current from 0 to 2 A. According to the training and testing results of the inverse force function, precise phase current is provided when phase current is larger than 1 A. Thus, the PSRM system mainly works at nonlinear magnetic field, and the inverse force function with good learning and generalization performances provides precise phase current command to current driver during online operation. Fig. 10 depicts the circular and quinquangular trajectory tracking responses of the PSRM system, and Figs. 11 and 12 show the position responses of X- and Y-axes for circular and quinquangular trajectories, respectively. From Figs. 10–12, under the inverse force function and PD controllers, the real circular trajectory Tc_{real} and quinquangular trajectory Tq_{real} coincide with the reference circular trajectory Tc_{ref} and quinquangular trajectory Tq_{ref}, respectively, and the PSRM system smoothly tracks the given circular and quinquangular trajectories since 2-D motions smoothly track their reference trajectories. Figs. 13 and 14 demonstrate the dynamic tacking errors of X- and Y-axes for circular and quinquangular trajectories, respectively. The figures clearly show that the PSRM system accurately tracks the circular and quinquangular trajectories, since the absolute
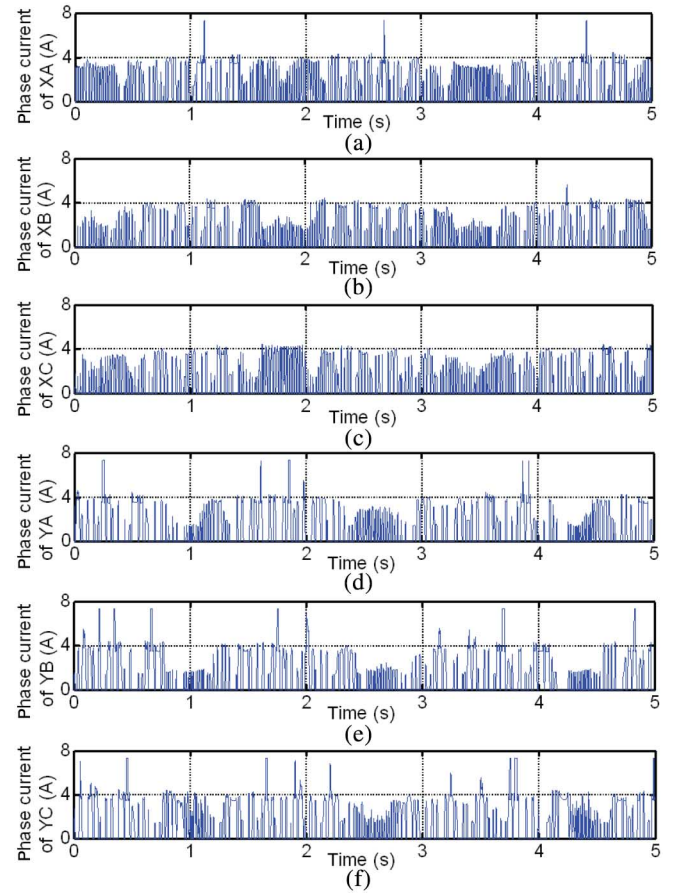

Fig. 8. Phase current commands of circular trajectory tracking. (a) Phase *XA*. (b) Phase *XB*. (c) Phase *XC*. (d) Phase *YA*. (e) Phase *YB*. (f) Phase *YC*.

values of dynamic tracking errors of circular and quinquangular trajectories are less than 48 and 46 μm, respectively.

C. Discussion

From the presented experimental results and aforementioned analysis, it comes to the conclusion that the PSRM system with the inverse force function provides precise phase current commands to current drivers in the presence of real-time operation and nonlinear magnetic characteristic, and the system exhibits satisfactory real-time performance and achieves precise planar motion for trajectory tracking. For the PSRM system with PD controller, the PD controllers have different parameters and the system has different performances in X- and Y-axes, since the mathematical models of control plant in both axes have identical form with different parameters, such as the different mass of moving platform and damping coefficient. Compared with the reported PSRM system for trajectory tracking [7], [34], the smallest reported absolute value of dynamic tracking error is less than 0.3 mm under a circular trajectory with a radius of 15 mm, while the absolute value of dynamic tracking error is less than 48 μm under a circular trajectory with a radius of 50 mm in this paper. Consequently, the PSRM system with the inverse force function achieves much higher dynamic position precision compared to the reported PSRM system. These research results demonstrate the feasibility and effectiveness of
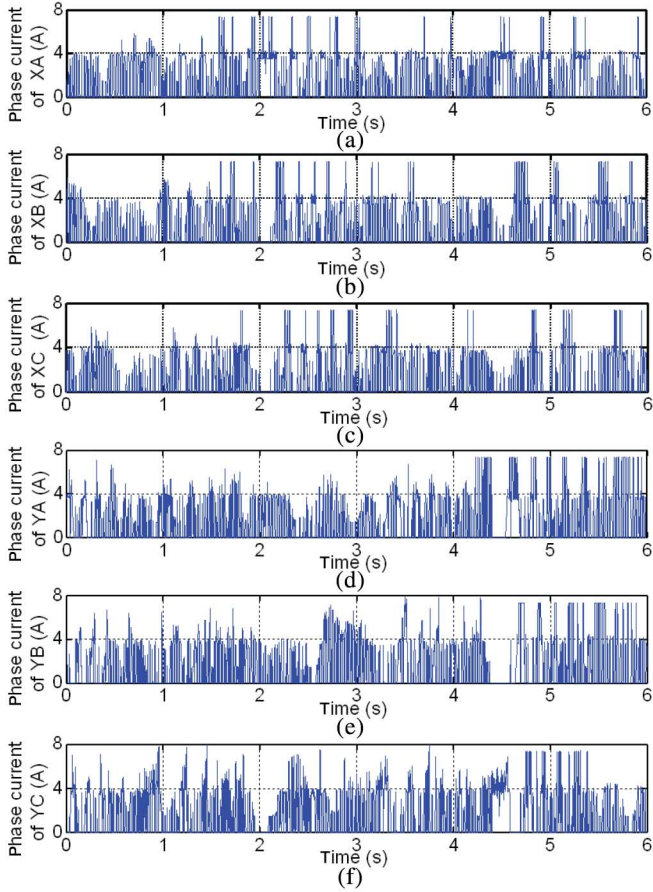
Fig. 9. Phase current commands of quinquangular trajectory tracking. (a) Phase *XA*. (b) Phase *XB*. (c) Phase *XC*. (d) Phase *YA*. (e) Phase *YB*. (f) Phase *YC*.
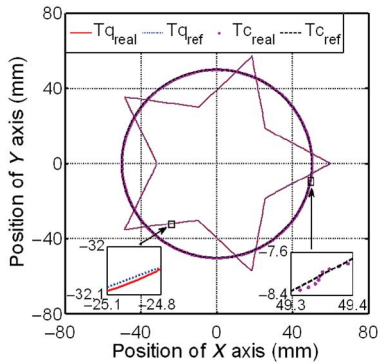

Fig. 10. Planar trajectory tracking responses of the PSRM system.
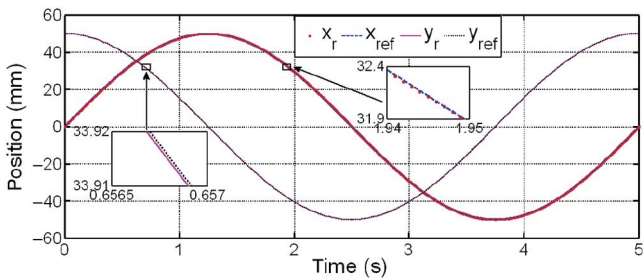

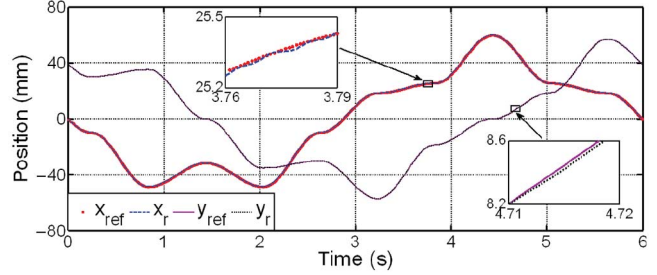Fig. 11. Position responses of *X*- and *Y*-axes for circular trajectory.

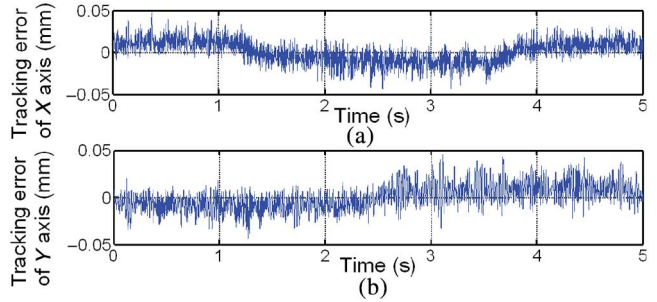Fig. 12. Position responses of *X*- and *Y*-axes for quinquangular trajectory.

Fig. 13. Dynamic tracking errors of circular trajectory. (a) *X*-axis. (b) *Y*-axis.
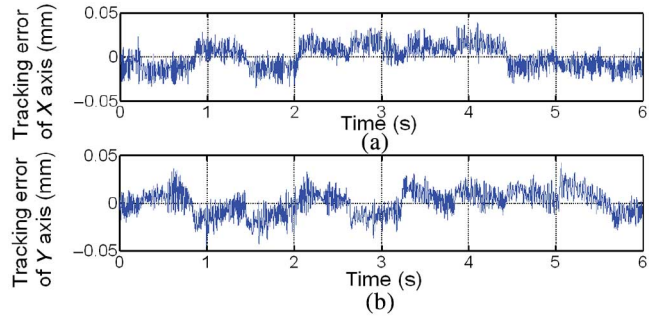

Fig. 14. Dynamic tracking errors of quinquangular trajectory. (a) *X*-axis. (b) *Y*-axis.

the inverse force function based on sparse LS-SVMs for the PSRM.

The inverse force function provides an accurate nonlinear modeling to achieve precise motion of the PSRM. The advantages of the function, in comparison with the conventional inverse force functions and nonlinear modeling based on ANNs, are mainly summarized as follows: 1) the powerful ability to accurately nonlinear modeling; 2) no requirement of high memory capacity for processor; and 3) the superior capability to deal with overfitting, small sample, local optima, and low arithmetic speed. Hence, the inverse force function can be readily implemented for real-time control application of PSRMs, and it is a recommended application with practicability for improving the dynamic position precision of PSRMs.

V. CONCLUSION

In this paper, a novel inverse force function using sparse LS-SVMs has been proposed to provide precise phase current command for precise motion of the PSRM. Compared with the conventional inverse force functions, the proposed function

exhibits potential ability to solve the problems of precise modeling based on complex nonlinear magnetic field and the requirement of high memory capacity for processor. The inverse force function has been modeled, tested, and applied to the PSRM system for trajectory tracking. Satisfactory performances of learning and generalization have been presented via training and testing results. Experimental results with superior real-time performance demonstrate that the PSRM system with the inverse force function outputs precise phase current commands in the presence of nonlinear magnetic characteristic, the absolute value of dynamic tracking error is less than $48~\mu m$, and the PSRM system achieves much higher dynamic position precision compared to the reported PSRM system. The proposed approach has shown its feasibility, validity, and promising industrial applicability, and provides a new way to accurately model the inverse force function of PSRMs for improving the dynamic position precision.

References

[1] M.-Y. Chen, H.-H. Huang, and S.-K. Hung, "A new design of a submicropositioner utilizing electromagnetic actuators and flexure mechanism," *IEEE Trans. Ind. Electron.*, vol. 57, no. 1, pp. 96–106, Jan. 2010.

[2] J. M. M. Rovers, J. W. Jansen, J. C. Compter, and E. A. Lomonova, "Analysis method of the dynamic force and torque distribution in the magnet array of a commutated magnetically levitated planar actuator," *IEEE Trans. Ind. Electron.*, vol. 59, no. 5, pp. 2157–2166, May 2012.

[3] L. Zhang, B. Kou, L. Li, and B. Zhao, "Modeling and design of an integrated winding synchronous permanent magnet planar motor," *IEEE Trans. Plasma Sci.*, vol. 41, no. 5, pp. 1214–1219, May 2013.

[4] J. M. M. Rovers, J. W. Jansen, and E. A. Lomonova, "Multiphysical analysis of moving-magnet planar motor topologies," *IEEE Trans. Magn.*, vol. 49, no. 12, pp. 5730–5741, Dec. 2013.

[5] J. W. Jansen, J. P. C. Smeets, T. T. Overboom, J. M. M. Rovers, and E. A. Lomonova, "Overview of analytical models for the design of linear and planar motors," *IEEE Trans. Magn.*, vol. 50, no. 11, Nov. 2014 [Online]. Available: http://ieeexplore.ieee.org/xpl/articleDetails.jsp?tp=&arnumber=6971593

[6] J. F. Pan and N. C. Cheung, "An adaptive controller for the novel planar switched reluctance motor," *IET Elect. Power Appl.*, vol. 5, no. 9, pp. 677–683, Nov. 2011.

[7] J. Pan, N. C. Cheung, and J. Yang, "High-precision position control of a novel planar switched reluctance motor," *IEEE Trans. Ind. Electron.*, vol. 52, no. 6, pp. 1644–1652, Dec. 2005.

[8] J. F. Pan, N. C. Cheung, W. C. Gan, and S. W. Zhao, "A novel planar switched reluctance motor for industrial applications," *IEEE Trans. Magn.*, vol. 42, no. 10, pp. 2836–2839, Oct. 2006.

[9] J. F. Pan, Y. Zou, and G. Cao, "Adaptive controller for the double-sided linear switched reluctance motor based on the nonlinear inductance modelling," *IET Elect. Power Appl.*, vol. 7, no. 1, pp. 1–15, Jan. 2013.

[10] J. F. Pan, N. C. Cheung, and Y. Zou, "An improved force distribution function for linear switched reluctance motor on force ripple minimization with nonlinear inductance modeling," *IEEE Trans. Magn.*, vol. 8, no. 11, pp. 3064–3067, Nov. 2012.

[11] S. W. Zhao, N. C. Cheung, W.-C. Gan, and J. M. Yang, "High-precision position control of a linear-switched reluctance motor using a self-tuning regulator," *IEEE Trans. Power Electron.*, vol. 25, no. 11, pp. 2820–2827, Nov. 2010.

[12] S. W. Zhao, N. C. Cheung, W.-C. Gan, J. M. Yang, and J. F. Pan, "A self-tuning regulator for the high-precision position control of a linear switched reluctance motor," *IEEE Trans. Ind. Electron.*, vol. 54, no. 5, pp. 2425–2434, Oct. 2007.

[13] W.-C. Gan, N. C. Cheung, and L. Qiu, "Position control of linear switched reluctance motors for high-precision applications," *IEEE Trans. Ind. Appl.*, vol. 39, no. 5, pp. 1350–1362, Sep./Oct. 2003.

[14] Z. Lin, D. S. Reay, B. W. Williams, and X. He, "Online modeling for switched reluctance motors using B-spline neural networks," *IEEE Trans. Ind. Electron.*, vol. 54, no. 6, pp. 3317–3322, Dec. 2007.

[15] O. Ustun, "Measurement and real-time modeling of inductance and flux linkage in switched reluctance motors," *IEEE Trans. Magn.*, vol. 45, no. 12, pp. 5376–5382, Dec. 2009.

[16] N. Cristianini and S.-T. John, *An Introduction to Support Vector Machines and Other Kernel-Based Learning Methods*. Cambridge, U.K.: Cambridge Univ. Press, 2003.

[17] D. You, X. Gao, and S. Katayama, "Multisensor fusion system for monitoring high-power disk laser welding using support vector machine," *IEEE Trans. Ind. Informat.*, vol. 10, no. 2, pp. 1285–1295, May 2014.

[18] G. Liu, L. Chen, W. Zhao, Y. Jiang, and L. Qu, "Internal model control of permanent magnet synchronous motor using support vector machine generalized inverse," *IEEE Trans. Ind. Informat.*, vol. 9, no. 2, pp. 890–898, May 2013.

[19] J.-C. Wang, C.-H. Lin, E. Siahaan, B.-W. Chen, and H.-L. Chuang, "Mixed sound event verification on wireless sensor network for home automation," *IEEE Trans. Ind. Informat.*, vol. 10, no. 1, pp. 803–812, Feb. 2014.

[20] P.-K. Wong, Q. Xu, C.-M. Vong, and H.-C. Wong, "Rate-dependent hysteresis modeling and control of a piezostage using online support vector machine band relevance vector machine," *IEEE Trans. Ind. Electron.*, vol. 59, no. 4, pp. 1988–2001, Apr. 2012.

[21] A. Bernieri, G. Betta, L. Ferrigno, M. Laracca, and S. Mastrostefano, "Multifrequency excitation and support vector machine regressor for ECT defect characterization," *IEEE Trans. Instrum. Meas.*, vol. 63, no. 5, pp. 1272–1280, May 2014.

[22] C. L. Bastard, Y. Wang, V. Baltazart, and X. Derobert, "Time delay and permittivity estimation by ground-penetrating radar with support vector regression," *IEEE Geosci. Remote Sens. Lett.*, vol. 11, no. 4, pp. 873–877, Apr. 2014.

[23] J. Zhao, Q. Liu, W. Pedrycz, and D. Li, "Effective noise estimation-based online prediction for byproduct gas system in steel industry," *IEEE Trans. Ind. Informat.*, vol. 8, no. 4, pp. 953–963, Nov. 2012.

[24] A. Soualhi, K. Medjaher, and N. Zerhouni, "Bearing health monitoring based on Hilbert–Huang transform, support vector machine, and regression," *IEEE Trans. Instrum. Meas.*, vol. 64, no. 1, pp. 52–62, Jan. 2015.

[25] M. Kang *et al.*, "Reliable fault diagnosis for low-speed bearings using individually trained support vector machines with kernel discriminative feature analysis," *IEEE Trans. Power Electron.*, vol. 30, no. 5, pp. 2786–2797, May 2015.

[26] Y.-H. Liu, H.-P. Huang, and C.-H. Weng, "Recognition of electromyographic signals using cascaded kernel learning machine," *IEEE/ASME Trans. Mechatronics*, vol. 12, no. 3, pp. 253–264, Jun. 2007.

[27] Q. Ye, Z. Han, J. Jiao, and J. Liu, "Human detection in images via piecewise linear support vector machines," *IEEE Trans. Image Process.*, vol. 22, no. 2, pp. 778–789, Feb. 2013.

[28] A. Ganapathiraju, J. E. Hamaker, and J. Picone, "Applications of support vector machines to speech recognition," *IEEE Trans. Signal Process.*, vol. 52, no. 8, pp. 2348–2355, Aug. 2004.

[29] R. Solera-Urena, A. I. Garcia-Moral, C. Pelaez-Moreno, M. Martinez-Ramon, and F. Diaz-de-Maria, "Real-time robust automatic speech recognition using compact support vector machines," *IEEE Trans. Audio Speech Lang. Process.*, vol. 20, no. 4, pp. 1347–1361, May 2012.

[30] J. A. K. Suykens and J. Vandewalle, "Least squares support vector machine classifiers," *Neural Process. Lett.*, vol. 9, no. 3, pp. 293–300, Jun. 1999.

[31] J. A. K. Suykens, L. Lukas, and J. Vandewalle, "Sparse approximation using least squares support vector machines," in *Proc. IEEE Int. Symp. Circuits Syst. (ISCAS)*, Geneva, Switzerland, May 2000, vol. 2, pp. 757–760.

[32] R. Krishnan, *Switch Reluctance Motor Derives: Modeling, Simulation, Analysis, Design, and Application*. Boca Raton, FL, USA: CRC Press, 2001.

[33] T. Petsche, S. J. Hanson, and J. Shavlik, *Computational Learning Theory and Natural Learning Systems: Selecting Good Models*. Cambridge, MA, USA: MIT Press, 1995.

[34] J. F. Pan, G.-Z. Cao, and N. C. Cheung, *Design and Control of Planar Motors*. Beijing, China: Science Press, 2011.

Su-Dan Huang received the B.Sc. and M.Sc. degrees in control theory and control engineering from Shenzhen University, Shenzhen, China, in 2009 and 2012, respectively. She is currently pursuing a joint Ph.D. degree in electrical engineering with the Southwest Jiaotong University, Chengdu, China, and the Shenzhen Key Laboratory of Electromagnetic Control, Shenzhen University, Shenzhen.

Her research interests include design and control of planar switched reluctance motors, and control theory and its application.
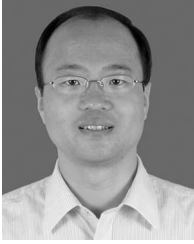
Guang-Zhong Cao (M'15) received the B.Sc., M.Sc., and Ph.D. degrees in electrical engineering and automation from Xi'an Jiaotong University, Xi'an, China, in 1989, 1992, and 1996, respectively.

He is currently a Professor and Director with the Shenzhen Key Laboratory of Electromagnetic Control, Shenzhen University, Shenzhen, China. He has authored more than 60 articles in refereed journals and conferences. His research interests include motor control, and control theory and its application.

Zheng-You He (M'10–SM'13) received the B.Sc. and M.Sc. degrees in computational mechanics from Chongqing University, Chongqing, China, in 1992 and 1995, respectively, and the Ph.D. degree in electrical engineering from Southwest Jiaotong University, Chengdu, China, in 2001.
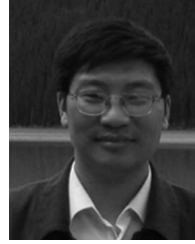
He is currently a Professor with the Department of Electrical Engineering, Southwest Jiaotong University. His research interests include signal processing and information theory applied to power system, and application of wavelet transforms in power system.

J. F. Pan received the B.Sc. degree in electrical engineering from the ChangChun University of Science and Technology, ChangChun, China, in 2001, and the Ph.D. degree in electrical engineering from Hong Kong Polytechnic University, Hong Kong, China, in 2006.

He is currently a Professor with the Shenzhen Key Laboratory of Electromagnetic Control, Shenzhen University, Shenzhen, China. His research interests include design and control of switched reluctance motors and generators.

Ji-An Duan received the Ph.D. degree in mechanical engineering from Xi'an Jiaotong University, Xi'an, China, in 1996.

He is currently a Professor and Director with the State Key Laboratory of High Performance Complex Manufactory, Central South University, Changsha, Hunan, China. He has authored more than 60 articles in refereed journals and conferences. His research interests include advanced manufacturing technology and equipment, and dynamics analysis and control of electromechanical system.

Qing-Quan Qian received the B.Sc. degree in electrical engineering from Southwest Jiaotong University, Chengdu, China, in 1960.

Since 1997, he has been an Academician with the Chinese Academy of Engineering, Beijing, China. He is currently a Professor with the Department of Electrical Engineering, Southwest Jiaotong University. His research interests include electrification and automation of rail transit.